Scripta Materialia 206 (2022) 114252

Contents lists available at ScienceDirect

Scripta Materialia

journal homepage: www.elsevier.com/locate/scriptamat

Single crystalline-like crystallographic texture formation of pure tungsten through laser powder bed fusion

Tsubasa Todo[a], Takuya Ishimoto[a,b], Ozkan Gokcekaya[a,b], Jongyeong Oh[a], Takayoshi Nakano[a,b,*]

[a] Division of Materials and Manufacturing Science, Graduate School of Engineering, Osaka University, 2-1, Yamadaoka, Suita, Osaka 565-0871, Japan
[b] Anisotropic Design & Additive Manufacturing Research Center, Osaka University, 2-1, Yamadaoka, Suita, Osaka 565-0871, Japan

ARTICLE INFO

Article history:
Received 20 April 2021
Revised 22 July 2021
Accepted 26 August 2021
Available online 11 September 2021

Keywords:
Laser powder bed fusion (LPBF)
Tungsten
Crystallographic texture
Densification
Simulation

ABSTRACT

We successfully formed the first prominent crystallographic texture of tungsten using laser powder bed fusion (LPBF). It is difficult even to manufacture highly dense tungsten products using LPBF because of its extremely high melting point and high thermal conductivity. By tuning the laser process parameters, we succeeded in fabricating almost fully dense pure tungsten parts with a relative density of 99.1%, which is the highest value yet to be reported. More importantly, a single crystalline-like prominent crystallographic texture evolved, in which <011> preferentially oriented in the scanning direction. This texture was formed to reduce the crystal misorientation at the melt pool center, at which the solidification fronts from the right and left halves of the melt pool encounter. This texture formation mechanism is similar to that of conventional alloys with ordinary thermal properties; however, the crystal growth directionality that governs the crystallographic orientation differs according to the melt pool morphology.

Tungsten has extremely high shape stability even at ultra-high temperatures owing to its extremely high melting point (3422°C) and low coefficient of thermal expansion; therefore, it has been widely used in the aerospace, medicine, and nuclear industries [1]. Tungsten has a body-centered cubic (BCC) structure and shows radiation damage resistance depending on the crystal plane, where {011} has a higher resistance than {100} or {111} [2]. Crystal orientation control gives tungsten high functionality. However, tungsten parts have been produced using powder metallurgy [3,4], which are unsuitable for complex shapes and controlled crystallographic microstructures. This is owing to its poor formability resulting from its brittleness at room temperature. Tungsten has a high ductility–brittle transition temperature (DBTT) of 200–400°C [5].

The grain boundary character distribution has a significant impact on the strength and ductility [6,7], cracking [8], and resistance to environment-assisted failure [9]. Tungsten shows crack initiation and propagation along high-angle grain boundaries (HAGBs) at ambient temperature owing to its high DBTT, which limits its high-density fabrication [10]. Thus, the prevention of high-energy grain boundary formation is necessary to improve crack resistance and density [11,12]. Microstructures with a prominent crystallographic texture, such as a single crystalline structure, can eliminate high-angle grain boundaries. Therefore, crystallographic texture formation is needed to densify the tungsten parts and promote its industrial application.

Laser powder bed fusion (LPBF) can produce highly dense components with complicated geometries in a net shape. In addition, recent studies have shown that LPBF is highly effective in controlling the crystallographic texture of various metallic materials—from randomly oriented polycrystalline to single crystalline-like microstructures [13,14]—and the resulting mechanical and chemical properties [15–19]. LPBF has been applied to refractory metals such as chromium [20], molybdenum [21], tantalum [22,23], and tungsten [12,24–27]. Previous studies [12,24–27] succeeded in producing relatively dense tungsten parts. The recently reported relative densities reached 98.58% [28] and 98.71% [29], which are much lower than those of titanium-, aluminum-, and iron-based alloys commonly used in LPBF. Moreover, LPBF-processed tungsten with the <011> single crystalline-like crystallographic texture, which ensures the highest radiation resistance, has yet to be achieved. The main factors hindering the densification of tungsten through LPBF are its high melting point, thermal conductivity, viscosity, and surface tension of the melt [24]. These factors significantly affect the melt-pool characteristics, such as the shape,

* Corresponding author at: Division of Materials and Manufacturing Science, Graduate School of Engineering, Osaka University, 2-1 Yamadaoka, Suita, Osaka 565-0871, Japan.
E-mail address: nakano@mat.eng.osaka-u.ac.jp (T. Nakano).

https://doi.org/10.1016/j.scriptamat.2021.114252

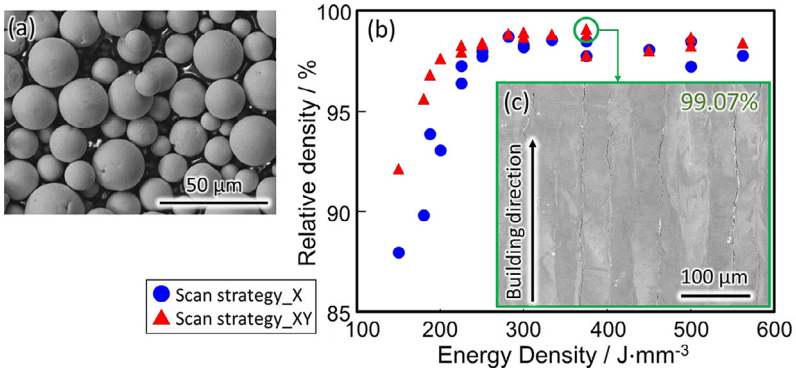

Fig. 1. (a) SEM image of raw tungsten powders, (b) relative density of fabricated products as a function of laser energy density, and (c) *yz*-cross-section of the sample showing the highest relative density.

size, and related solidification behavior (thermal gradient, direction and migration rate of the liquid/solid interface) in a melt pool, which governs crystallographic texture formation in the LPBF process [18,30]. The strategy for texture formation in tungsten differs greatly from that in other frequently used metallic materials. Hence, the formation and control of the crystallographic texture in tungsten through LPBF is a challenge. We attempted the densification of pure tungsten and crystallographic texture control to overcome the fragility at the grain boundaries by optimizing the laser conditions in LPBF.

Pure spherical tungsten powder with >99.9% purity prepared using inductively coupled plasma (Tekna Advanced Materials Inc., Canada) was applied (Fig. 1(a)). The average powder particle size measured using a Mastersizer 3000 (Malvern Panalytical, UK) was 27.4 µm. The fluidity of the powder was measured using a Revolution powder analyzer (Mercury Scientific, USA). The powder showed excellent fluidity with rest and avalanche angles of 25.5° and 32.4°, respectively. Specimens with dimensions of 5 mm (depth) × 5 mm (length) × 10 mm (height) were fabricated using an LPBF apparatus (EOS M290, EOS, Germany) with laser power, scanning speed, scan pitch, and layer thickness of 360 W, 600–1200 mm/s, 40–100 µm, and 20 µm, respectively. The fabrication was performed in an Ar atmosphere. The baseplate was preheated and maintained at 200°C. Two types of scanning strategies were used: bidirectional (zigzag) scanning along the *x*-axis (Scan Strategy_X) and bidirectional scanning with a rotation of 90° between layers (Scan Strategy_XY) [17]. The density of the fabricated specimens was measured using Archimedes' method (LA310S, Sartorius, Germany), and the relative density was calculated based on the absolute density of tungsten, 19.25 g/cm^3. The microstructures were analyzed using a field-emission scanning electron microscope (JIB-4610F, JEOL, Japan) and an electron backscatter diffraction system (NordlysMax^3, Oxford Instruments, UK).

To compare the texture formation mechanism in tungsten with that of the titanium alloy, for which we previously succeeded in acquiring a single crystalline-like texture [17], a numerical simulation of the thermal diffusion behavior was conducted (COMSOL Multiphysics® 5.5, COMSOL Inc., USA). The size and shape of the melt pool and the heat flow direction during laser scanning were analyzed. Laser heat sources are modeled using a Gaussian distribution [31], which is expressed as follows:

$$Q = \frac{4AP}{\pi R^2 H}\exp\left(-\frac{2r^2}{R^2}\right)\left[1-\frac{z}{H}\right] \quad (0 < z < H) \tag{1}$$

where Q is the amount of heat per unit volume, P is the laser power, R is the laser spot radius (50 μm) [32], r is the distance from the powder bed surface to the center of the laser spot, A is the laser absorption rate, H is the penetration depth, and z is the depth. In addition, A and H are the fitting parameters, the reliability of which is ensured by comparing the simulated melt-pool shape with the actual one [33].

Table 1
Physical and thermophysical parameters of pure tungsten and titanium used in the simulations.

Physical parameters	Unit	Tungsten	Titanium
Density	g/cm^3	19.25	4.51
Melting point	K	3695	1941
Thermal conductivity		174	17
Heat capacity	J/(kg·K)	138	610

The dimensions of the finite element model were 5 (width) × 5 (depth) × 5 (height) mm (Supplementary Fig. 1S). The heat source ran at the center of the top surface along the *x*-direction. The laser energy absorption efficiency of the powder bed was higher than that of the bulk surface because of multiple scattering on the powder particle surface. In this calculation, the powder bed was not modeled, but the energy absorption rate A was set to 85% [31] to consider the high heat absorptivity of the powder bed. The convection in the melt pool is not calculated in this study. Instead, the surface energy flux absorption model in which Gaussian heat flux attenuated with penetration depth is deposited on the top surface was adopted. This model is one of the most adopted models in the finite element simulation of LPBF [34]. This simplification has a relatively small effect on the melt pool size and temperature gradients [34]. For example, the consideration of convection in addition to thermal conduction resulted in a reduction of the melt pool depth by approximately 10% [35]. The detailed calculation conditions are described in the Supplementary file. Table 1 lists the thermophysical properties of the materials used in the simulations. In this study, the temperature dependency of these properties was not taken into account because the temperature-dependent variation in the properties was smaller than the difference between the two materials.

Fig. 1(b) shows the variation in the relative density of the fabricated specimens as a function of the volumetric laser energy density, defined as

$$E = \frac{P}{v \cdot d \cdot t}, \tag{2}$$

where P is the laser power, v is the scanning speed, d is the pitch distance, and t is the layer thickness. The sample manufactured using Scan Strategy_XY (green circle in Fig. 1(b)) showed a relative density of 99.07%, the highest density reported. The SEM image of the *yz*-cross-section of the highest-density specimen is shown in Fig. 1(c). Although some cracks running parallel to the building direction were observed, few pores were observed. These cracks are caused by the residual stress accumulated in the fabricated spec-

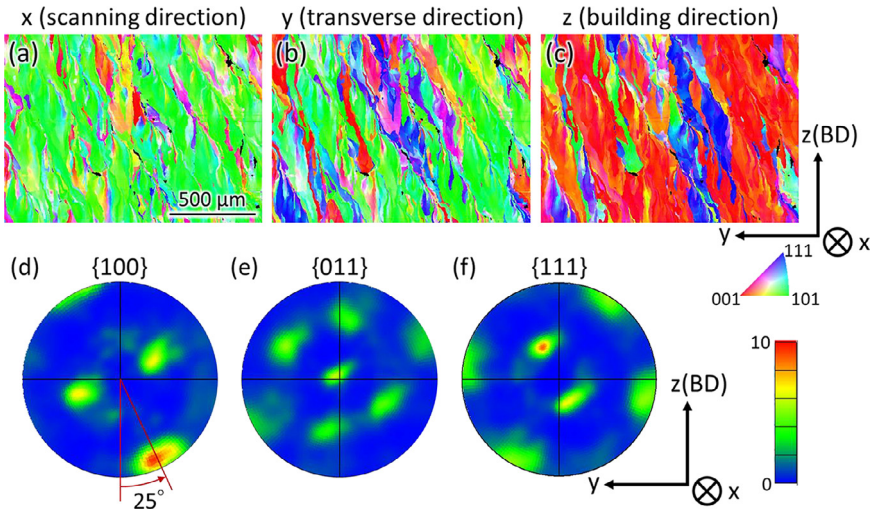

Fig. 2. IPF orientation map projected in the (a) scanning *x*-direction, (b) transverse *y*-direction, and (c) building *z*-direction, and the corresponding pole figures for (d) {100}, (e) {011}, and (f) {111}.

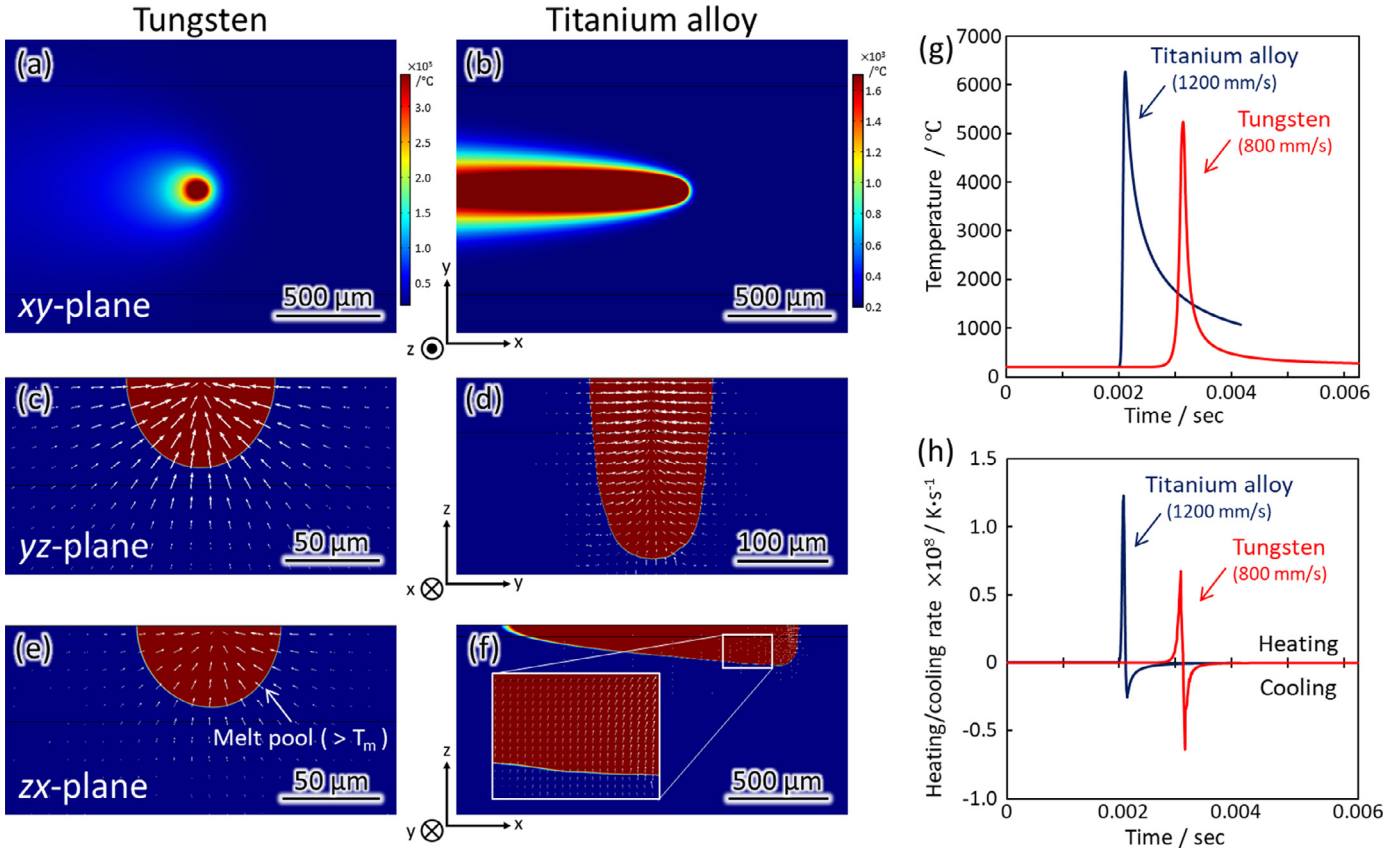

Fig. 3. (a, b) Temperature distribution on *xy*-plane and melt pool geometries on (c, d) *yz*- and (e, f) *xz*-planes with heat flow directions of (a, c, e) tungsten and (b, d, f) titanium alloy. (g) Temperature variation and (h) cooling rate over time for a location at mid-length on *xy*-plane of tungsten and titanium alloy. Note that the scales are different in images.

imen and the ductile nature of tungsten at ambient temperature [36]. Crack-sensitive HAGBs must be eliminated to prevent crack initiation and propagation; thus, a single crystalline-like texture should be beneficial.

Fig. 2 shows the crystallographic texture of a specimen fabricated under P = 360 W, v = 800 mm/s, d = 40 µm, and Scan Strategy_X. Pole figures (Fig. 2(d)–(f)) show clear symmetry of the cubic structure, indicating a single crystal-like texture formation. The texture tilts in the *yz*-plane by approximately 25° counterclockwise from the building direction toward the subsequent scan track direction. Therefore, the inverse pole figure (IPF) maps for the *y*- (Fig. 2(b)) and *z*-axes (Fig. 2(c)) were drawn by projecting crystallographic orientations along the 25°-tilted direction. The rotation of the crystal orientation is because only half of the melt pool remains as the distance between adjacent tracks (scan pitch) is small. The evolved texture is char-

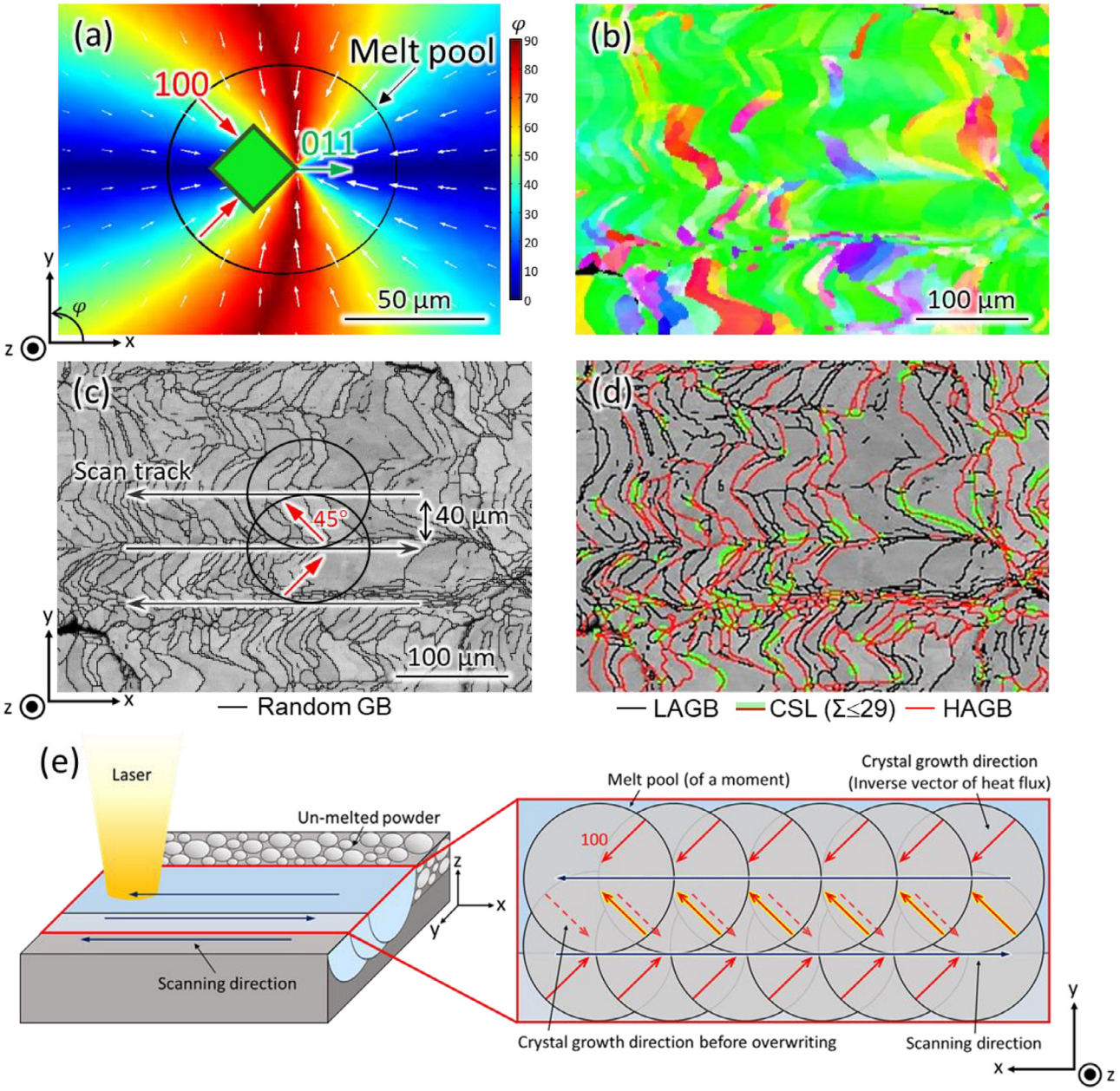

Fig. 4. Color map of (a) heat flow direction on *xy*-plane of tungsten. (b) IPF orientation map in the scan direction (*x*-direction) on *xy*-plane with (c) random grain boundary and (d) grain boundary character distribution. (e) Illustration of crystal growth directions during tungsten fabrication by LPBF with respect to melt pool shape and pitch space.

acterized as a <011>//scanning *x*-direction, <011>//transverse *y*-direction, and <100>//building *z*-direction. Although the formation of <111>//building direction fiber texture in LPBF was reported [36], forming a single crystalline-like cubic texture in tungsten by the LPBF process was achieved for the first time herein. The single crystalline-like texture is beneficial for exposing the radiation damage-resistant {011} while simultaneously eliminating high-angle grain boundaries to suppress crack formation.

The texture formed in tungsten is completely different from that typically observed in other cubic metals, such as titanium-based alloys [17], nickel-based alloys [37], and stainless steel [18]. The texture with <100> along the scanning *x*-direction and <011> along the building *z*-direction is commonly obtained under Scan Strategy_X (Supplementary Fig. S2) [17]. Recent reports have indicated that the melt pool shape significantly impacts the crystallographic texture evolution [18,30]. We considered that the extremely high melting point and thermal conductivity of tungsten largely affect the melt pool shape (melting and solidification behavior) during laser irradiation owing to heat dissipation. Therefore, a numerical simulation was conducted to analyze the thermal diffusion behavior during laser scanning, focusing on the differences in thermophysical properties between tungsten and titanium alloy as a representative material for LPBF. For tungsten, a laser power of $P = 360$ W and a scan speed of $v = 800$ mm/s were used for the simulation, which evolved the strong texture shown in Fig. 2. For the titanium alloy, a laser power of $P = 360$ W and scan speed of $v = 1200$ mm/s were used for the simulation, which successfully achieved a single crystalline-like texture where <100> and <011> oriented in the scanning *x*-direction and building *z*-direction of the as-built component, respectively [17].

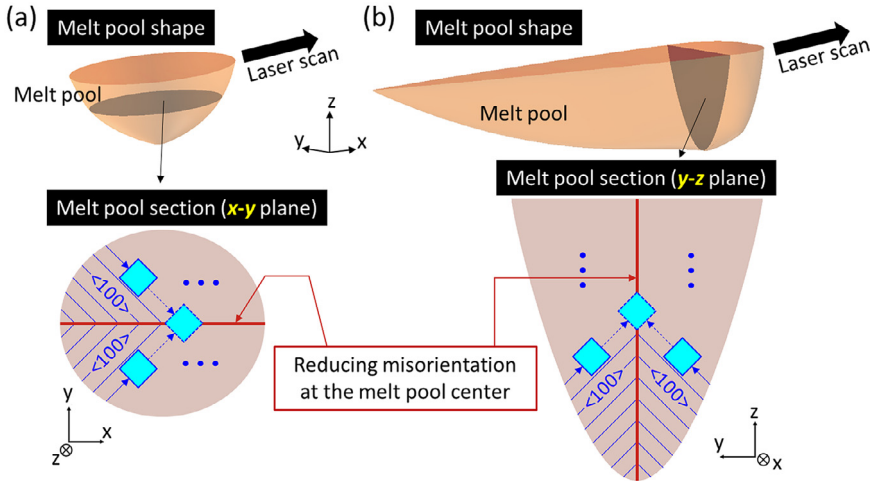

Fig. 5. Schematic illustrations of melt pool formed through laser scan for (a) tungsten and (b) titanium alloy. Two-dimensional <100> growth (solid–liquid interface movement) occurs in the *xy*-and *yz*-planes, respectively, in tungsten and titanium alloys, and the crystal orientation is adjusted such that a misorientation becomes smaller at the center of the melt pool in these planes. Blue lines indicate <100> direction, and blue squares schematically indicate cubic crystal lattice.

Fig. 3 compares the numerical simulation outcomes of the tungsten and titanium alloys. There are remarkable differences in the temperature distribution (Fig. 3(a, b, g)), melt pool shape and related heat flow direction (Fig. 3(c–f)), and heating/cooling rate (Fig. 3(h)). Owing to its high melting point and thermal conductivity, tungsten showed rapid heat removal and a resultant small and hemisphere-shaped melt pool. In contrast, the titanium alloy exhibited a larger melt pool with a long tail. The "long tail" is crucial for the texture formation in titanium alloy because it enables a two-dimensional heat flow and the related migration of the solid–liquid interface in the *yz*-plane, resulting in two-dimensional <100>-oriented columnar cell growth in the *yz*-plane, as experimentally demonstrated [17,38], thereby resulting in grain boundaries with a slight misorientation at the melt pool center.

In a hemisphere-shaped melt pool generated in tungsten, a two-dimensional heat flow and a solid–liquid interface migration in the *yz*-plane could not be realized, and the texture formation through the mechanism in titanium alloy was not achieved, indicating the necessity of considering the texture formation dominated by other modes of heat flow and solid–liquid interface migration.

Fig. 4 shows the crystallographic texture formation focusing on the heat flow (Fig. 4(a)) and microstructure (Fig. 4(b)) in the *xy*-plane. According to the simulation, the heat flow direction varies from 0° to 90° from the scanning *x*-direction in the *xy*-plane (Fig. 4(a)). However, microstructural observation revealed a 45° inclined crystal grain with an <100> orientation in the elongated direction, from the scanning *x*-direction, in each track. Hence, the crystallographic misorientation at the melt pool center (in the *xy*-plane), where the solidification fronts of the right- and left-side encounter, can be decreased in the same way as seen in the *yz*-plane in titanium alloy [17,38]. This misorientation resulted in a unique crystallographic texture, where <011> was oriented in the *x*- and *y*-directions and <100> was oriented in the *z*-direction.

The heat flow angle in the scanning *x*-direction on the simulated *xy*-plane is shown in Fig. 4(a). A black line represents the outline of the melt pool. The melt pool showed a nearly circular shape, resulting in an average heat flow of 45° from the scanning *x*-direction. Many grain boundaries at 45° from the *x*-direction were observed on the *xy*-plane of the sample (Fig. 4(b,c)), strongly suggesting that the heat flow in this direction was dominant in the texture formation. In summary, because of the <100> growth at an angle of 45° from the *x*-direction on the *xy*-plane in the right and left halves of the melt pool, <110> is preferentially oriented in the *x*- and *y*-directions, as shown by the green cube in Fig. 4(a), and <100> was fixed in the *z*-direction. In the next laser scan track that overwrites the previously solidified track, the 45°-tilted <100> orientation can be inherited by epitaxial growth (Fig. 4(e)), leading to the formation of a single crystalline-like texture, as shown in Fig. 2. As a result of the intense crystallographic texture formation of well-aligned neighboring grains, HAGB connectivity was disrupted by LAGB and a coincidence site lattice (CSL; Brandon criterion $\Sigma \leq 29$) (Fig. 4(d)), which prevented the occurrence of cracking and improved densification.

Finally, the mechanism of a single crystalline-like texture formation in tungsten under the LPBF process compared with that of the titanium alloy is shown in Fig. 5. In tungsten, the 45°-tilted <100> growth from the scanning *x*-direction in the *xy*-plane governed the texture formation, where <011> is oriented in the *x*- and *y*-directions. In the titanium alloy, the 45°-tilted <100> growth from the building *z*-direction in the *yz*-plane predominates the texture formation, where <011> orients in the *y*- and *z*-directions. The formation of these different orientations is determined by the shape of the melt pool, which is largely governed by the thermophysical properties of the material. In either case, it is possible that the driving force is to reduce the crystal misorientation at the melt pool center, where the solidification fronts from the right and left halves of the melt pool encounter.

This texture formation mechanism for tungsten (Fig. 5(a)) could apply to the fabrication under Scan Strategy_XY because the 45°-tilted <100> growth from the scanning direction in the *xy*-plane determines the texture in which the *x*- and *y*-scanning directions are equivalent. In fact, in the specimen fabricated under Scan Strategy_XY, a texture like that fabricated under Scan Strategy_X was formed, as shown in Supplementary Fig. S3, which, however, requires further tuning of the laser conditions for a more prominent texture.

The insights obtained in this research suggest a new texture control method using the LPBF. Furthermore, by changing the process parameters and/or materials, a new type of single crystalline-like texture is expected to be obtained, which can be predicted and discussed using numerical simulation. If a slight difference in the melt pool shape or solidification behavior is the subject of discussion, a more rigorous simulation that considers the thermal

conductivity of the powder bed, temperature dependence of the thermophysical properties, and consideration of convection are required.

Declaration of Competing Interest

The authors declare that they have no known competing financial interests or personal relationships that could have appeared to influence the work reported in this paper.

Acknowledgment

Funding: This work was supported by Grants-in-Aid for Scientific Research (JP18H05254) from the Japan Society for the Promotion of Science (JSPS). This work was also partly supported by the Cross-Ministerial Strategic Innovation Promotion Program (SIP), Materials Integration for Revolutionary Design System of Structural Materials, Domain C1: "Development of Additive Manufacturing Process for Ni-based Alloy" from the Japan Science and Technology Agency (JST).

Supplementary materials

Supplementary material associated with this article can be found, in the online version, at doi:10.1016/j.scriptamat.2021.114252.

References

[1] L. Huang, L. Jiang, T.D. Topping, C. Dai, X. Wang, R. Carpenter, C. Haines, J.M. Schoenung, Acta. Mater. 122 (2017) 19–31.
[2] F. Maury, M. Biget, P. Vajda, A. Lucasson, P. Lucasson, Radiat. Eff. 38 (1978) 53–65.
[3] E. Lassner, W.D. Schubert, Tungsten: Properties, Chemistry, Technology of the Element, Alloys, and Chemical Compounds, Springer, US, 2012.
[4] J. Ma, J. Zhang, W. Liu, Z. Shen, J. Nucl. Mater. 438 (2013) 199–203.
[5] S.W.H. Yih, W. Yih, C.T. Wang, Tungsten: Sources, Metallurgy, Properties, and Applications, Springer, US, 1979.
[6] T. Watanabe, H. Fujii, H. Oikawa, K.I. Arai, Acta. Metall. 37 (1989) 941–952.
[7] V. Randle, Acta. Mater. 52 (2004) 4067–4081.
[8] P. Kontis, E. Chauvet, Z. Peng, J. He, A.K. da Silva, D. Raabe, C. Tassin, J.-J. Blandin, S. Abed, R. Dendievel, B. Gault, G. Martin, Acta. Mater. 177 (2019) 209–221.
[9] H. Kokawa, M. Shimada, M. Michiuchi, Z.J. Wang, Y.S. Sato, Acta. Mater. 55 (2007) 5401–5407.
[10] A. Iveković, N. Omidvari, B. Vrancken, K. Lietaert, L. Thijs, K. Vanmeensel, J. Vleugels, J.-P. Kruth, Int. J. Refract. Met. Hard Mater. 72 (2018) 27–32.
[11] I.M. Mikhailovskij, T.I. Mazilova, V.N. Voyevodin, A.A. Mazilov, Phys. Rev. B 83 (2011) 134115.
[12] D. Wang, Z. Wang, K. Li, J. Ma, W. Liu, Z. Shen, Mater. Des. 162 (2019) 384–393.
[13] O. Gokcekaya, T. Ishimoto, S. Hibino, J. Yasutomi, T. Narushima, T Nakano, Acta. Mater. 212 (2021) 116876.
[14] T. Ishimoto, S. Wu, Y. Ito, S.-H. Sun, H. Amano, T. Nakano, ISIJ Int (2020) 1758–1764.
[15] Q. Chao, V. Cruz, S. Thomas, N. Birbilis, P. Collins, A. Taylor, P.D. Hodgson, D. Fabijanic, Scr. Mater. 141 (2017) 94–98.
[16] Y. Zhang, J. Zhang, Q. Yan, L. Zhang, M. Wang, B. Song, Y. Shi, Scr. Mater. 148 (2018) 20–23.
[17] T. Ishimoto, K. Hagihara, K. Hisamoto, S.-H. Sun, T. Nakano, Scr. Mater. 132 (2017) 34–38.
[18] S.-H. Sun, T. Ishimoto, K. Hagihara, Y. Tsutsumi, T. Hanawa, T. Nakano, Scr. Mater. 159 (2019) 89–93.
[19] O. Gokcekaya, N. Hayashi, T. Ishimoto, K. Ueda, T. Narushima, T. Nakano, Addit. Manuf. (2020) 101624.
[20] O. Gokcekaya, T. Ishimoto, T. Todo, R. Suganuma, R. Fukushima, T. Narushima, T. Nakano, Crystals 11 (2021) 9.
[21] M. Higashi, T. Ozaki, Mater. Des. 191 (2020) 108588.
[22] L. Thijs, M.L. Montero Sistiaga, R. Wauthle, Q. Xie, J.-P. Kruth, J. Van Humbeeck, Acta. Mater. 61 (2013) 4657–4668.
[23] J. Yang, X. Jin, H. Gao, D. Zhang, H. Chen, S. Zhang, X. Li, Mater. Charact. 170 (2020) 110694.
[24] C. Tan, K. Zhou, W. Ma, B. Attard, P. Zhang, T. Kuang, Sci. Technol. Adv. Mater. 19 (2018) 370–380.
[25] A.v. Müller, G. Schlick, R. Neu, C. Anstätt, T. Klimkait, J. Lee, B. Pascher, M. Schmitt, C. Seidel, Nucl. Mater. Energy 19 (2019) 184–188.
[26] Z. Xiong, P. Zhang, C. Tan, D. Dong, W. Ma, K. Yu, Adv. Eng. Mater. 22 (2020) 1901352.
[27] Z. Hu, Y. Zhao, K. Guan, Z. Wang, Z. Ma, Addit. Manuf. 36 (2020) 101579.
[28] T. Yamamoto, M. Hara, Y. Hatano, Int. J. Refract. Met. Hard Mater. 95 (2021) 105410.
[29] S. Wen, C. Wang, Y. Zhou, L. Duan, Q. Wei, S. Yang, Y. Shi, Opt. Laser Technol. 116 (2019) 128–138.
[30] O. Andreau, I. Koutiri, P. Peyre, J.-D. Penot, N. Saintier, E. Pessard, T. De Terris, C. Dupuy, T. Baudin, J. Mater. Process. Technol. 264 (2019) 21–31.
[31] A. Takase, T. Ishimoto, N. Morita, N. Ikeo, T. Nakano, Crystals 11 (2021) 796.
[32] Q. Chen, X. Liang, D. Hayduke, J. Liu, L. Cheng, J. Oskin, R. Whitmore, A.C. To, Addit. Manuf. 28 (2019) 406–418.
[33] M.-S. Pham, B. Dovgyy, P.A. Hooper, C.M. Gourlay, A. Piglione, Nat. Commun. 11 (2020) 749.
[34] H.J. Willy, X. Li, Z. Chen, T.S. Herng, S. Chang, C.Y.A. Ong, C. Li, J. Ding, Mater. Design 157 (2018) 24–34.
[35] G.L. Knapp, N. Raghavan, A. Plotkowski, T. DebRoy, Addit. Manuf. 25 (2019) 511–521.
[36] A.T. Sidambe, Y. Tian, P.B. Prangnell, P. Fox, Int. J. Refract. Met. Hard Mater. 78 (2019) 254–263.
[37] S.-H. Sun, K. Hagihara, T. Nakano, Mater. Des. 140 (2018) 307–316.
[38] T. Ishimoto, K. Hagihara, K. Hisamoto, T. Nakano, Addit. Manuf. 43 (2021) 102004.